Industrial Crops & Products 224 (2025) 120317

Contents lists available at ScienceDirect

Industrial Crops & Products

journal homepage: www.elsevier.com/locate/indcrop

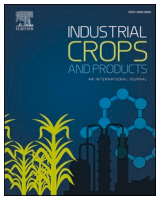

The role of nitrogen and sulfur doping in the peroxymonosulfate activation of cobalt-immobilized *Polygonatum kingianum* dregs biochar

Fali Hou [b,c,d], Jinli Zhai [b,c,d], Jiali Yan [b,c,d], Kaiying Yang [b,c,d], Wei Li [b,c,d], Min Li [a], Weimei Yu [a], Xiaoya Gao [b,c,d,*], Xingxin Yang [a,**]

[a] College of Pharmaceutical Science, Yunnan University of Chinese Medicine, 1076 Yuhua Road, Kunming 650500, PR China
[b] Faculty of Environmental Science and Engineering, Kunming University of Science and Technology, Kunming 650500, PR China
[c] The Innovation Team for Volatile Organic Compounds Pollutants Control and Resource Utilization of Yunnan Province, Kunming 650500, PR China
[d] The Higher Educational Key Laboratory for Odorous Volatile Organic Compounds Pollutants Control of Yunnan Province, Kunming 650500, PR China

ARTICLE INFO

Keywords:
Polygonatum kingianum dregs biochar
Cobalt encapsulation
Heteroatoms
Peroxymonosulfate
Degradation

ABSTRACT

Biomass wastes from agriculture are very important sources to fabricate high-value materials for water purification. Herein, we encapsulated cobalt inside *Polygonatum kingianum* (PK) dregs biochar with no doping and the doping of N, S, and N-S to investigate the roles of Co/N/S in promoting the catalytic activity on activating peroxymonosulfate (PMS) to degrade emerging pollutant. Cobalt nanoparticles were evenly wrapped in the carbon matrix by N doping, leading to no apparent cobalt nanoparticles in Co@BC-N and presenting a poorer activity. Additionally, Co was converted to Co_9S_8 (Co@BC-S) and Co_4S_3 (Co@BC-N,S) by S doping and N-S co-doping, respectively. Particularly, both the experiments and DFT calculations revealed an outstanding synergistic effect between Co_4S_3 and the N-S co-modified carbon matrix, which significantly raised the adsorption of PMS and activated it into non-radical ($^1O_2$ and electron transfer) and radical pathways ($SO_4^{\bullet-}$, •OH, and $O_2^{\bullet-}$). The Co@BC-N,S/PMS system completely degraded carbamazepine (CBZ) within 20 min, with an apparent rate constant (k_{app}) of 2.7, 16.0, and 19.6 times higher than that of Co@BC-S, Co@BC, and Co@BC-N, respectively. Furthermore, this system exhibited good tolerance to environmental matrix, great effectiveness in actual water body, and high degradation efficiency of CBZ in five cycles. Overall, this work not only bridged the knowledge gap of the connections between structural properties of the modified Co@BC hybrid and catalytic performance, but also introduced a new view for utilization of PK dregs in catalytic decontamination.

1. Introduction

As an important traditional Chinese herb, *Polygonatum kingianum* (PK) mainly cultivated in Southwest China has been used as traditionally medicinal and functional food for centuries (Yang et al., 2019; Zhang et al., 2024). The PK possesses extensive pharmacological activities, including immunity promotion, anti-aging, blood glucose reduction, and lipid regulation. It has been verified in modern studies that these activities are highly related to the content of polysaccharides and steroidal saponins, which were the main substances in the rhizome of PK (Mu et al., 2021; He et al., 2022). Furthermore, its extract is widely used in clinical, health food, and daily chemical products. With the wide industrialization, it will inevitably generate a large number of dregs with 170,000 tons one year in China. Therefore, improper disposal of PK dregs will inevitably lead to resources waste and environment pollution.

Nowadays, biomass is proposed as a kind of vital precursor for the preparation of biochar-based catalysts to be used in water purification, which is a good way to reach the object of "treating waste with waste" (Zhu et al., 2023; Xu et al., 2024). Compared to conventional biomass such as corn stover, PK dregs undergo specific planting and manufacturing methods. Hence, using PK dregs to prepare biochar is more easily to construct a standardized form of "feedstock-production-property-application". Therefore, it is worth studying the application potential of PK dregs biochar-based catalysts in catalytic decontamination.

Peroxymonosulfate-based advanced oxidation processes (PMS-AOPs) has gained increasing attention in catalytic decontamination because of the superiorities of multiple oxidation pathways, high

* Corresponding author at: Faculty of Environmental Science and Engineering, Kunming University of Science and Technology, Kunming 650500, PR China.
** Corresponding author.
E-mail addresses: gaoxiaoyaya@126.com (X. Gao), yxx78945@163.com (X. Yang).

https://doi.org/10.1016/j.indcrop.2024.120317
Received 19 October 2024; Received in revised form 25 November 2024; Accepted 10 December 2024

contaminants removal efficiency, and stable oxidant involvement (Li et al., 2021; Zhang et al., 2022). Generally, PMS can be activated into radical and non-radical oxidation processes through catalytic activation. The high efficiency of radical induced oxidation leans on the high activity of $SO_4^{\bullet-}$ (2.5–3.1 V) and •OH (1.9–2.7 V) whose redox potential is more higher than $SO_5^{\bullet-}$ (1.1 V) and $O_2^{\bullet-}$ (0.56 V) (Li et al., 2023; Xie et al., 2023). However, the oxidation efficiency will be affected by the background organics/inorganics, limiting its practical application in the complex water environment (Wacławek et al., 2017; Hodges et al., 2018). Alternately, non-radical systems mostly induced by $^1O_2$ and electron transfer process (ETP) feature excellent anti-interference, high selectivity for electron-rich pollutants, and high utilization efficiency of peroxide (Ren et al., 2022). Therefore, the strategy of integrating radical and non-radical induced oxidation has received more and more attention (Qu et al., 2022; Xiao et al., 2022). Notably, when it comes to developing a novel catalyst to trigger multiple oxidation pathways, opportunities and challenges come together.

Currently, numerous biochar materials have been developed and used in PMS activation. Nonetheless, the overall performance of the original biochar in PMS activation needs to be improved because of the limited catalytic sites and poor stability (Dou et al., 2022; Shi et al., 2022; Dung et al., 2024). A variety of strategies have been developed to enhance the performance of biochar-based material. Among them, encapsulating mental nanoparticles (MNPs) inside carbon matrix is a novel strategy for preparing highly efficient carbon-based catalysts (Tang et al., 2019; Otor et al., 2020). In general, the stable carbon matrix is also called chain-mail for catalyst to protect the inner from harsh reaction conditions (Yu et al., 2020). And the outer carbon layer can be activated via the electronic interactions between the inner MNPs and carbon, leading the redistribution of electrons in the hybrid, which is crucial for us to rationally design highly-efficient catalysts. Moreover, it has been proposed that doping heteroatoms into carbon matrix can significantly affect the redistribution of electrons as well as the activity of the hybrid (Dai et al., 2016; Yu et al., 2020). Particularly, N-S co-doping generally can realize synergy effect caused by the redistribution of spin/charge densities and the production of new catalytic sites. For example, Duan et al. revealed that the apparent rate constant (k_{app}) of N-S co-doped rGO in activation of PMS for phenol removal is of 4.5, 19.7, and 22.8 times than that of N-rGO, S-rGO, and rGO, respectively (Duan et al., 2015), and Du et al. found that, in comparison with Co@NC, the performance of Co-S@NC displayed a 1.71-fold improvement in dinotefuran degradation (Du et al., 2020).

We herein encapsulated metal cobalt inside biochar with no doping and the doping of N, S, and N-S through one-pot pyrolysis process, by using PK dregs as the carbon precursor. For comparison, pure biochar and N and S co-doped biochar were also prepared. The main objectives of this study are aimed to: (1) synthesize and characterize the Co@BC hybrids with no doping and the doping of N, S, and N-S; (2) examine the role of heteroatoms doping in prompting the catalytic activity of biochar; (3) investigate the utilization potentiality of the optimal Co@BC-N,S/PMS system. This study fills the knowledge gap of the roles of N or/and S doping in changing the structural properties of Co@BC hybrids and further affecting the catalytic performances/PMS activation pathways of the hybrids, which will promote the environmental applications of biochar-based catalysts.

2. Materials and methods

2.1. Reagents and analytical methods

The regents are analytical grade or above. The detailed information of regents is shown in Text S1 of the Supporting Information. Furthermore, the analytical methods and computational details are given in Text S2 and Text S3, respectively.

2.2. Synthesis of catalysts

The PK dregs were obtained from Yunnan Province, China. The dregs were dried in an oven (80℃) and the dried dregs were smashed into small particles less than 80 mesh by a grinder. Then the obtained powder was collected for further use. Catalysts were synthesized using the modified in-situ impregnation-pyrolysis process (Feng et al., 2022). The detailed processes of preparing Co@BC-N,S are given in Text S4.

2.3. Experimental procedures

The synthesized materials were used to activate PMS for catalytic decontamination of carbamazepine (CBZ). PMS activation experiments were performed in a 100 mL beaker containing a given concentration of CBZ, PMS, and catalyst, which was conducted at 25℃. The beginning pH of the reaction system was about 6.8 and need no further adjustment. At specific time intervals, 0.5 mL of suspension was collected and filtered via a syringe filter (0.45 μm) for subsequent testing. Reactive oxygen species (ROS) were determined through quenching experiments as well as electron paramagnetic resonance (EPR). The effects of pH, coexisted anions (NO_3^-, SO_4^{2-}, HPO_4^{2-}, Cl^-, and HCO_3^-) and humic acid (HA) on the catalytic decontamination of CBZ were studied in detail. Three parallel experiments were conducted in each group with error bars shown in all figures.

3. Results and discussion

3.1. Characterization of catalysts

As shown in Fig. 1, the crystal structures of all as-prepared materials in this study were studied by X-ray diffraction (XRD) firstly. It displayed that graphitic carbon (2θ=26.6°) (PDF#01–075–2078) and SiO_2 (PDF#97–003–9830) were the common phases in all samples. For Co@BC, these diffraction peaks at 44.2, 51.5, and 75.8° were matched with the (111), (200), and (220) planes of cobalt (PDF#00–015–0806) (Liu et al., 2022). Interestingly, diverse crystallographic phases of cobalt were discovered in Co@BC series materials through different types of heteroatoms doping. Specifically, as shown in the enlarged XRD patterns of Co@BC and Co@BC-N (Fig. S1), there were no apparent diffraction peaks of Co nanoparticles in the Co@BC-N due to the doping of N. It has been reported that cobalt (Lewis acid) was susceptible to bind with N (Lewis base) to form robust Co–N coordination in the carbon matrix

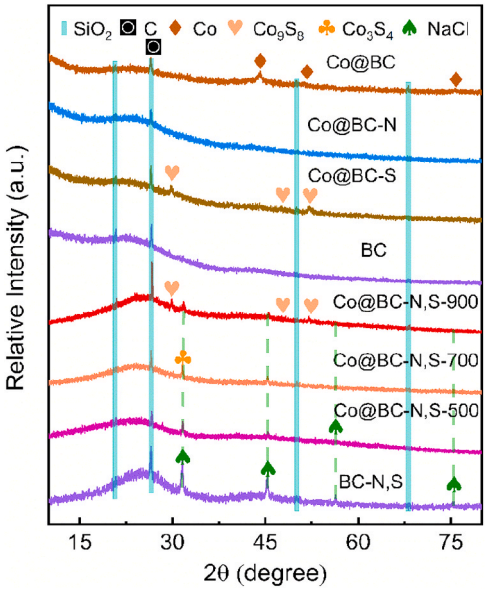

Fig. 1. XRD patterns of all materials.

(Wang et al., 2019). Here, this result might suggest the success in nitrogen doping, and that the doped N could better isolate and stabilize the cobalt atoms through strong Co–N coordination structure. In addition, cobalt sulfides substituted for cobalt nanoparticles with the doping of S (Co@BC-S). The peaks at 29.8, 47.5, and 52.0° could be ascribed to the (311), (511), and (440) planes of Co_9S_8 (PDF#00–056–0002) (Navarro Pardo et al., 2020). For N and S co-doping, cobalt nanoparticles were replaced by Co_3S_4, and the peak at 31.5° corresponded to the (311) plane of Co_3S_4 (PDF#00–047–1738) (Navarro Pardo et al., 2020). Above results indicated that N doping, S doping, and N-S doping significantly affected the existential state of the cobalt species.

Meanwhile, the XRD patterns of Co@BC-N,S at different annealing temperature were also investigated (Fig. 1). Clearly, the diffraction intensity of graphitic C (26.6°) gradually increased with the increasing calcination temperature, which was in accord with prior report (Wu et al., 2022). The XRD patterns of Co@BC-N,S were basically unchanged when the calcining heat was lower than 900 °C. However, the peaks of Co_3S_4 turned weak with temperature increasing to 900 °C, and the emerging characteristic peaks at 29.8, 47.5, and 52.0° could be indexed to Co_9S_8 (PDF#00–056–0002). For comparison, N and S co-doped BC was also prepared as the control sample. Surprisingly, the characteristic peaks of NaCl (PDF#01–070–2509) were identified in all N-S co-doped materials, which might be explained by the complexity of inherent components in biochar and the complex chemical environment resulting from N and S co-doping.

Fig. 2 displayed the surface morphologies of Co@BC-N,S calcinated at different temperature. As observed, the morphologies of Co@BC-N,S series materials were characterized with layered structure, irregular shape, and pore structure. Remarkably, the big blocks gradually broke up into a lot of unshaped small lumps with rising of temperature, and well-developed pore structure was formed at higher temperature, showing that the increasing calcining temperature significantly changed the structures and morphologies of the materials.

After that, the microstructures of the novel material Co@BC-N,S were surveyed by transmission electron microscopy (TEM) (Fig. 3a). Clearly, the carbon matrix of Co@BC-N,S-700 displayed multilayered structure, which met the SEM results (Fig. 2). Furthermore, there were some nanoparticles with a diameter of 10–25 nm and irregularly shaped black shadow areas with a diameter of 50–300 nm embedded in the carbon matrix. According to the enlarged images, the magnified images with interspacing of 0.18 nm could be observed, corresponding to the (2−12) plane of SiO_2 (Fig. 3a_1). The magnified black area with the lattice distance of 0.28 and 0.54 nm could be indexed to the (311) and (111) facets of Co_3S_4 (Fig. 3a_2) (Li et al., 2020). Additionally, the TEM elemental mappings of Co@BC-N,S-700 were given in Fig. S2. Results not only showed that N, S, and Co were evenly distributed on the surface of Co@BC-N,S-700 and successfully doped into the catalyst, but also confirmed the presence of other elements in the compounds mentioned in the above XRD analyses.

Fig. 3b showed the Raman spectra of all materials. The peaks at near 1350 cm^{-1} (D band) and 1580 cm^{-1} (G band) were identified in all materials, which could be indexed to the sp^2-bonded carbon within structural defects or disordered graphite and the ordered hexagonal lattice of graphite, respectively. And the intensity ratio of D to G band (I_D/I_G) was applied to measure the defect level of graphite-based materials (Tam et al., 2020; Sajjadi et al., 2021). As displayed in Fig. 3b_1, in comparison with BC (0.85), encapsulating cobalt nanoparticles inside biochar slightly elevated the defecting degree of Co@BC (0.9). Likewise, compared with Co@BC, the defecting degree was slightly elevated by heteroatoms doping except for Co@BC-S (0.89), which was in agreement with the previous study (Feng et al., 2022).

The Raman spectra of Co@BC-N,S calcinated at different temperature were also investigated (Fig. 3b_2). It showed that a higher temperature (>700 ℃) significantly increased the defecting degree. While the degree of defects no longer changed significantly when calcining heat increased to 900 °C. Compared with other materials, it was obvious that Raman spectrum of 500 °C showed a strong 2D band at about 2800 cm^{-1}, suggesting a high degree of stacking in the material (Hristea et al., 2024). According to the layered structure identified in the Fig. 2 and Fig. 3a, therefore, the 2D band might reflect the carbon layer thickness (Sajjadi et al., 2021). Clearly, the intensity of 2D peak gradually decreased with the increasing temperature, indicating the dropping carbon layer thickness. This was consistent with the results of SEM that big carbon blocks gradually broke up into a lot of unshaped small lumps (Fig. 2). As regards these catalysts (encapsulating metal nanoparticles inside carbon), the catalytic activity is strongly associated with the thickness of the carbon layer, which will be discussed in the Section 3.2 in detail.

To better understand the effects of heteroatoms doping on the physicochemical properties of catalysts, the valence states of elements were surveyed by X-ray photoelectron spectroscopy (XPS). Fig. S3 displayed the full XPS spectra of all materials, and it further confirmed the presence of the elements referred above. The deconvoluted XPS spectra of C 1 s and Co 2p of Co@BC with different heteroatoms doping were displayed in Fig. 4, and that of other samples and elements were given in Figs. S4–7.

The C 1 s spectra of all materials were showed in Fig. 4a and Fig. S4, which showed that there was an obvious difference between the samples with S doping and without. The C 1 s spectra of the samples without S doping could be ascribed to C–C (284.8 eV), C–O–C (286.4 eV), and O–C═O (288.8 eV) (Huang et al., 2022), while that with S doping could be divided into C–C (284.8 eV), C–O/C–N (286.1 eV), C–S (287.1 eV), C═O (288.5 eV), and π–π* shake up (290.5 eV) (Ma et al., 2021; Yu et al., 2020). Due to the complexity and relatively low intensity of the

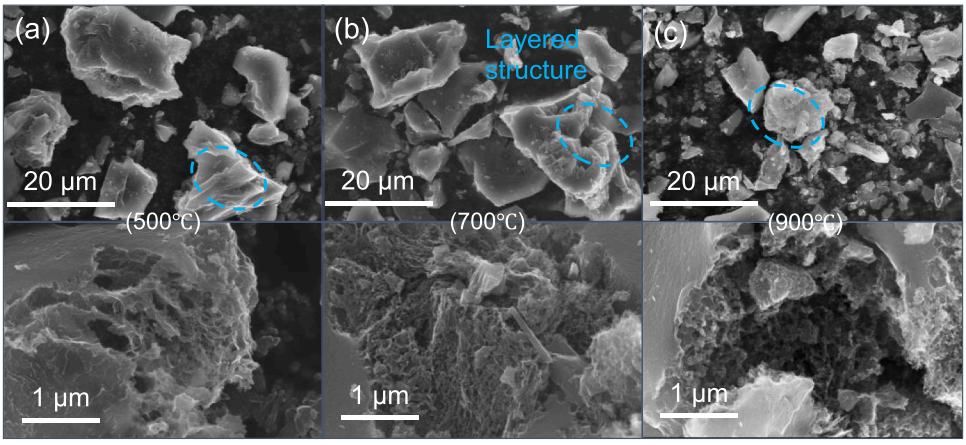

Fig. 2. SEM images of Co@BC-N,S calcinated at: (a) 500 ℃, (b) 700 ℃, and (c) 900 ℃.

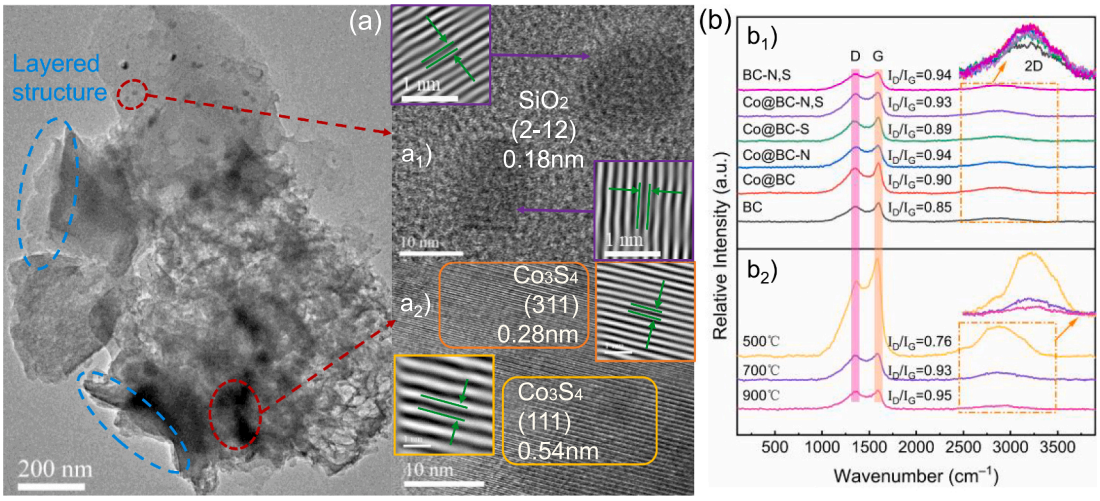

Fig. 3. (a) TEM images of Co@BC-N,S (Co@BC-N,S-700) and (b) Raman spectra of all synthetic materials.

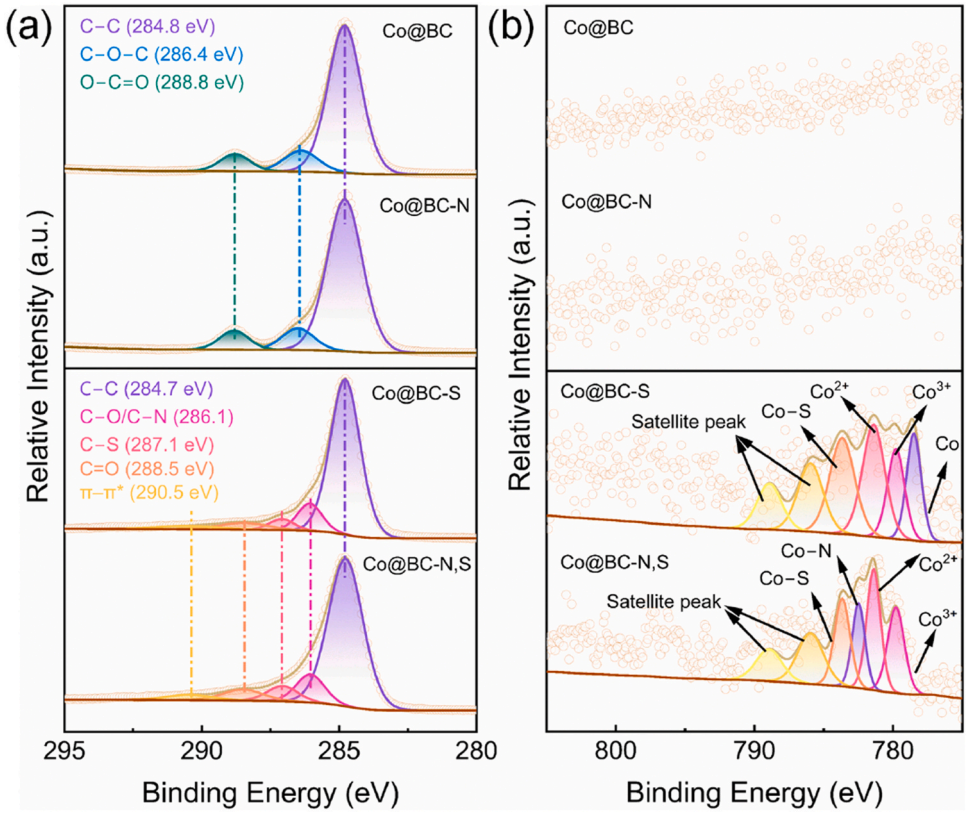

Fig. 4. Deconvoluted XPS spectra of Co@BC with different heteroatoms doping: (a) C 1 s and (b) Co 2p.

broad shoulder (286–291 eV), it is challenging and prone to errors to quantitatively analyze the contributions of various functional groups of that shoulder. By comparison, investigations of the O 1 s, N 1 s, and S 2p spectra are more straightforward. As displayed in Fig. S5, the O 1 s spectra of all samples showed that there was also an obvious difference between the samples with S doping and without. Moreover, as shown in Table S1, only the content of O in the materials with S doping presented a significant decrease. Above results indicated that more oxygen groups were removed, thus leading to a stronger π–π stacking, which was in line with the prior study (Duan et al., 2015).

For the N 1 s, as shown in Fig. S6, the peaks at 398.5, 400.1, 401.1, and 402.5 eV in the N 1 s spectra of all samples were ascribed to pyridinic N, pyrrolic N, graphitic N, and oxidized N (Wu et al., 2023). In contrast to Co@BC, the content of N in Co@BC-N increased by 53.2 %, among which the content of Pyridinic N increased by 151.6 % while that of Graphitic N and Pyrrolic N presented a slight change (Table S1). It was reported that, the more N content was added, the more Pyridinic N would be present in the graphitic layers, forwarding cobalt species being better immobilized in carbon layer (Du et al., 2020). Which further indicated that cobalt species might be encapsulate in carbon matrix by N atoms, being in line with the XRD result of Co@BC-N (Fig. 1). As for the S 2p spectra of all materials with S doping (Fig. S7), the peaks at 161.8, 163.7/164.81, and 168.0/169.2 eV were matched with the S^{2-}, C–S–C, and C–SO_x–C, among which the presence of S^{2-} could be ascribed to the

metal sulfides (Wang et al., 2020; Wang and Wang, 2020).

Furthermore, the Co 2p spectra of Co@BC with different heteroatoms doping were showed in Fig. 4b. There were no obvious Co 2p peaks for the Co@BC and Co@BC-N. The poor signal could be explained by the limited analysis depth of XPS (≤10 nm) (Wu et al., 2020). It is worth noting that all as-prepared materials have the same initial cobalt doping content. However, the Co 2p spectra of Co@BC-S and Co@BC-N,S could be resolved into Co (778.5 eV), Co^{3+} (779.8 eV), Co^{2+} (781.4 eV), Co–N (782.5 eV), Co–S (783.7 eV), and satellite peak (785.9/788.9 eV) (Wang and Wang, 2020; Song et al., 2023), suggesting that S doping contributed the formation of cobalt sites.

3.2. CBZ removal performance in different systems

CBZ is an emerging pollutant with degradation efficiencies of less than 10 % in global sewage treatment. Nowadays, CBZ was frequently detected in varied environmental water body, even in drinking water, which makes CBZ a possible anthropogenic marker in the water environment (Clara et al., 2004). The bioaccumulation and biomagnification of CBZ would cause serious toxic damage to the human health. Therefore, CBZ was selected as the model pollutant to further understand how heteroatom doping affects the physicochemical properties and PMS activation activity of all as-prepared catalysts.

As shown in Fig. 5a and Fig. S8, the control experiments illustrated that CBZ removal efficiency was less than 5.4 % when only PMS or catalyst was in the reaction solution, suggesting that single PMS and catalyst itself were ineffective for elimination of CBZ. For metal-free catalytic systems, the BC/PMS and BC-N,S/PMS only could achieve 12.6 % and 3.0 % CBZ removal within 40 min, respectively, which demonstrated that both of them possessed poor catalytic activity either pure BC or even the modified BC endowed with abundant surface functional groups through N and S co-doping (Figs. S4–7).

In comparison with the above two metal-free catalytic systems, the cobalt doping slightly increased the catalytic performance of Co@BC (35.4 %) with apparent rate constant (k_{app}) at 0.011 min^{-1}, revealing the important role of the doped cobalt in promoting catalytic activity. The insufficient catalytic activity of Co@BC might be explained by the low content of cobalt sites existing on the catalyst's surface and the poor physicochemical properties of pristine biochar. Interestingly, for the modified Co@BC materials, the N doping was unfavorable whilst S doping was favorable for the catalytic activity. Considering the significant role of the doped cobalt, we surprisingly discovered that there was a good linear relationship between k_{app} (Co@BC, Co@BC-N, and Co@BC-S) and the cobalt content (Fig. 5b, R^2 = 0.981). This further confirmed the indispensable role of the doped cobalt, and suggested that N doping inhibited the formation of cobalt active sites with the result of lower k_{app} (0.009 min^{-1}) while S doping contributed to the formation of cobalt sites resulting in a higher k_{app} (0.065 min^{-1}). With the presentence of Co@BC-N,S (Fig. 5c), however, the R^2 was reduced to 0.538. Notably, the k_{app} value of Co@BC-N,S (0.176 min^{-1}) was 2.7, 16.0, and 19.6 times higher than that of Co@BC-S, Co@BC, and Co@BC-N, respectively. Generally, the doped N not only could better isolate and stabilize the cobalt atoms through strong Co–N coordination structure, but also heighten the adsorption of PMS because of the enhancive surface basicity. This could contribute to electron transfer towards PMS, leading to the enhanced catalytic activity (Wang et al., 2019). Based on the results of above characterization and activity, for Co@BC-N, the negative effect of N doping might be explained by the Co–N structure being deeply embedded in the carbon matrix, exposing relatively low amount of cobalt sites on the surface; as to Co@BC-N,S, the positive effect might be caused by the synergistic effect of the high-reactivity Co_4S_3 nanoparticles and potential active sites in biochar (C═O groups, C–S–C, etc.).

As displayed in Fig. 5d and Fig. S8, the target pollutant catalytic performances of Co@BC-N,S calcined at 500, 700, and 900 ℃ were also investigated. It manifested that both the adsorption and catalytic performances of Co@BC-N,S were notably elevated with the increasing calcining temperature. For the adsorption performance, the catalysts achieved 0.5 %, 2.5 %, and 46.8 % CBZ removal within 40 min, respectively for the Co@BC-N,S calcined at 500, 700, and 900 ℃. And the greatly strengthened adsorption capacity might be ascribed to the rich porous structure (Fig. 2a) formed at the higher calcination temperature (900 ℃). Meanwhile, it was reported that the doped N could

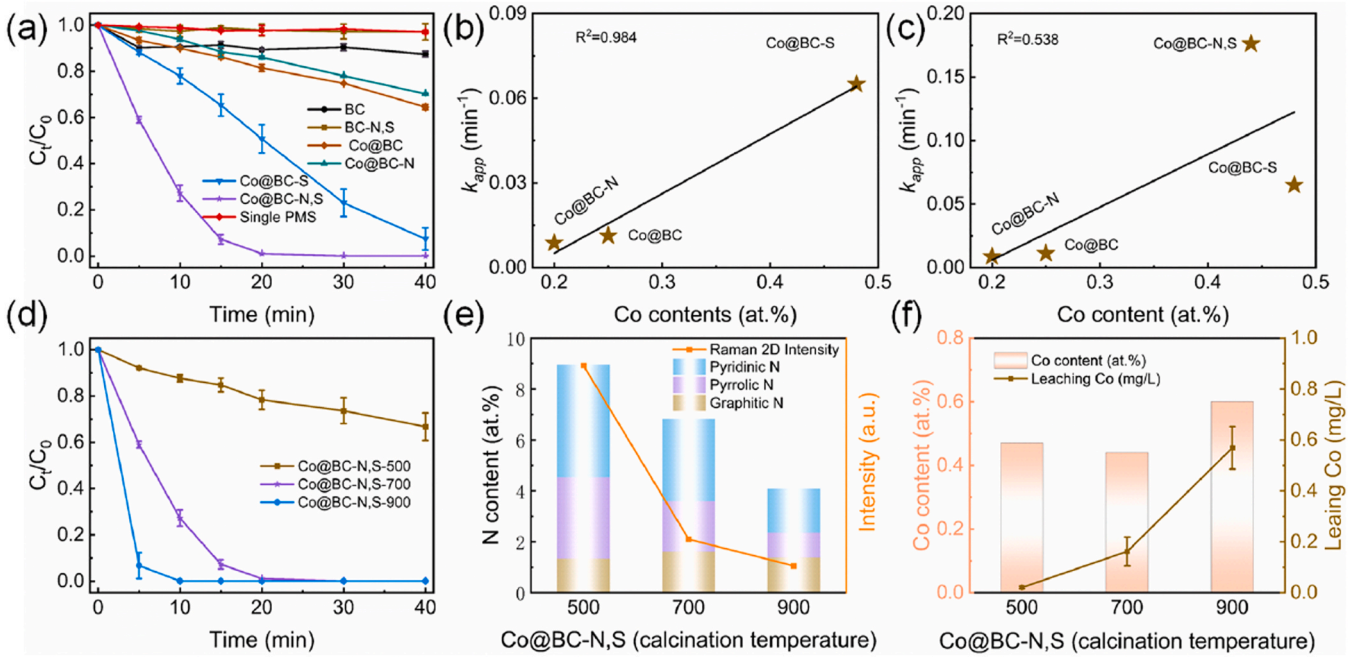

Fig. 5. (a) CBZ removal curves of N/S/Co modified BC, (b) and (c) linear correlation of cobalt contents (at%) and k_{app} of N and/or S doped Co@BC samples, (d) CBZ removal degradation curves of Co@BC-N,S at different calcinated temperature, (e) N contents (at%) and Raman 2D intensity of different Co@BC-N,S materials, and (f) Co contents (at%) in different Co@BC-N,S materials and cobalt leaching control experiments of different Co@rGO-N,S materials. Experiment conditions: [CBZ] = 2.5 mg/L, [Catalyst] = 0.1 g/L, [PMS] = 0.3 mM, and initial pH = 6.8.

stabilize cobalt and effectively restrain from cobalt leaching. As discussed above, the intensity of Raman 2D peak represents the thickness of carbon layer that is closely related to the catalytic activity and stability. Fig. 5e and f displayed that both the N content and 2D peak intensity of Co@BC-N,S decreased with the increasing temperature, while the cobalt content appeared an opposite trend. Clearly, the 900 ℃ showed a higher removal efficiency than the 700 ℃ (Fig. 5d), but it's cobalt leaching (0.57 mg/L) was significantly higher than that of 700 ℃ (0.16 mg/L, Fig. 5f). Although the rising temperature promoted the formation of porous structure attributed to the decomposition of biomass constituents, it might be prone to damage the material morphology and break up carbon matrix (Fig. 2a), resulting in too thin carbon layer to stabilize cobalt. In general, the leaching of cobalt ions is inevitable for Co-containing catalyst. However, the leaching of too much metal ions could be harmful to the environment and human health. Moreover, the loss of metal ions may affect the stability of catalyst. Here, the Co@BC-N,S-700 exhibited wonderful catalytic performance and had acceptable and a small number of cobalt ions leaching, therefore, it was chosen as the optimal catalyst.

As displayed in Fig. S9, experiment parameters (PMS and catalyst) of the Co@BC-N,S/PMS system were optimized. Under the optimal conditions of 0.1 g/L of catalyst and 0.3 mM of PMS, the Co@BC-N,S/PMS system could almost completely degrade CBZ (1–5 mg/L), and possess great degradation efficiency (81.1 %) to 7.5 mg/L of CBZ. Moreover, the comparison of catalytic activities of Co@BC-N,S and the reported metal@BC catalysts was given in Table S6. It showed that, in contrast to other metal@BC catalysts, the Co@BC-N,S prepared by encapsulating cobalt nanoparticles inside *Polygonatum kingianum* dregs biochar displayed greater catalytic performance.

3.3. Catalytic mechanism in Co@BC-N,S/PMS system

3.3.1. Identification of oxidation processes

Generally, PMS could be activated into radical and non-radical oxidation processes, which could be modulated by the physicochemical characteristics of materials (Ren et al., 2022; Yan et al., 2023). Furthermore, previous studies have displayed that both the two processes could be induced by heteroatoms/metal-doped carbon through activating persulfate (Yan et al., 2023). Considering the diversity of the physicochemical features of Co@BC-N,S discussed above, both the radical oxidation process driven by •OH, $SO_4^{\bullet-}$, and $O_2^{\bullet-}$ and non-radical oxidation process mostly induced by $^1O_2$ and ETP were systematically investigated.

As for the common ROS, firstly, the trapping agents ρ-benzoquinone (ρ-BQ), furfuryl alcohol (FFA), tert-butanol (TBA), and methanol (MeOH) were added into the system. TBA, ρ-BQ, and FFA could be employed to quench •OH, $O_2^{\bullet-}$, and $^1O_2$, respectively, while MeOH could capture both •OH and $SO_4^{\bullet-}$ (Miao et al., 2020). Fig. S10 demonstrated that the concentrations of scavengers were optimized for quenching corresponding ROS.

Accordingly, 50 mM TBA was applied to quench •OH, and 50 mM MeOH was suitable for quenching both •OH and $SO_4^{\bullet-}$. Additionally, 1 mM ρ-BQ and FFA were used to quench $O_2^{\bullet-}$ and $^1O_2$, respectively. As displayed in Fig. 6a, the total CBZ removal efficiency was slightly impeded under 50 mM TBA, while the catalytic degradation of CBZ was almost stopped in the presence of MeOH, ρ-BQ, and FFA. Results suggested that •OH played a relatively minor role while the $SO_4^{\bullet-}$, $O_2^{\bullet-}$, and $^1O_2$ possessed a critical role for catalytic decontamination. Armed with TEMP and DMPO, respectively for trapping $^1O_2$ and $O_2^{\bullet-}$/•OH/$SO_4^{\bullet-}$, the involvements of above ROS were further confirmed by EPR (Fig. 6b–d). Clearly, there were almost no EPR signals in pure PMS solution, while the corresponding EPR signals of the four ROS were detected in the Co@BC-N,S/PMS system, being in accord with the quenching results. Moreover, the increasing peak tensity of the ROS signals suggested that the Co@BC-N,S could continuously decompose PMS for the generation of ROS being responsible to remove pollutants.

Meanwhile, it has been reported that premixed experiment could offer the supporting evidence for non-radical pathways (Chen et al.,

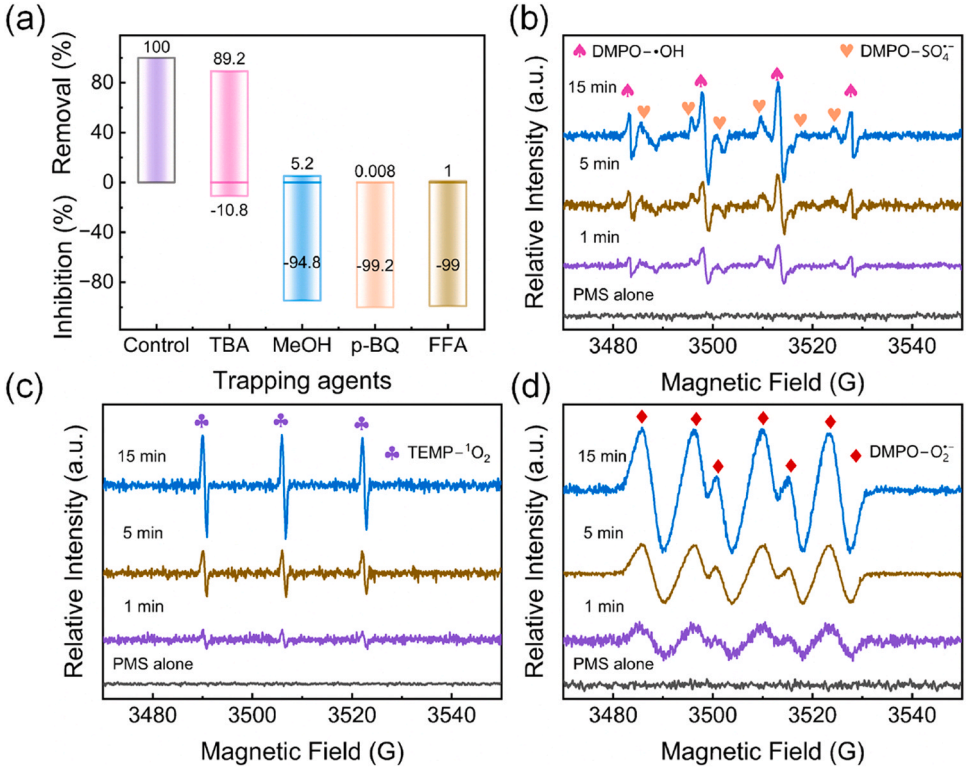

Fig. 6. (a) Effects of the quenchers on CBZ removal and the EPR spectra of (b) •OH and $SO_4^{\bullet-}$, (c) $^1O_2$, and (d) $O_2^{\bullet-}$. Experiment conditions: [CBZ] = 2.5 mg/L, [Catalyst] = 0.1 g/L, [PMS] = 0.3 mM, and initial pH = 6.8.

2023; Zhao et al., 2023). Typically, the removal rate of the systems dominated by non-radical oxidation processes can't be severely affected by premixing time. As depicted in Fig. 7a, the removal rate at different premixing time (5 and 10 min) decreased to varying degree. However, the CBZ removal performance didn't vary basically when the premixing time exceeded 20 min. These results further confirmed that the system could continue to produce ROS before 15 min, being in consistent with the EPR results, and indicated that ETP might be involved in the catalytic process. ETP usually could be classified into two groups: electrons shuttle and adjacent transfer. It has been reported that the transfer of electrons from pollutants to PMS/catalyst complexes through a conductive bridge (electrons shuttle) was the primary process for conductive materials (noble metals and carbons). Besides, ETP could be started as the redox potential of the catalyst (E_{cat}) exceeds the oxidation potential of organics (E_{org}) (Ren et al., 2022).

Subsequently, some electrochemical techniques were utilized to identify the involvement of ETP. As depicted in Fig. 7b, the potentials of the complexes were got by open circuit potential (OCP). The equilibrium potential of PMS/Co@BC-N,S was significantly higher than that of PMS/Co@BC-S, suggesting that Co@BC-N,S had a better affinity for PMS. As displayed in Fig. S11, meanwhile, the PMS decomposition experiments showed that the Co@BC-N,S (22 %) possessed higher PMS decomposition than Co@BC-S (14 %), which was in line with the results of OCP. And then, the above acquired potentials were used as the applied potential for chronoamperometry (CP) analysis with the addition of PMS at 400 s and subsequently adding of CBZ at 600 s. Fig. 7c demonstrated that Co@BC-N,S had a stronger negative response current than Co@BC-S, moreover, only the Co@BC-N,S/PMS system displayed a positive current signal after the addition of CBZ. This not only suggested that ETP was involved in the Co@BC-N,S/PMS system (Yang et al., 2020), but also indicated the fact that ETP could be induced when $E_{cat} > E_{org}$. Moreover, the charge transfer capacities of Co@BC-S and Co@BC-N,S were explored by electrochemical impedance spectroscopy (EIS). The smaller radius of semicircle means the greater conductivity of the catalysts (Qin et al., 2022), as shown in Fig. 7d. It indicated that the N and S co-doping observably elevated the conductivity of Co@BC-N,S, leading to a higher electron transfer efficiency, which met above analysis.

3.3.2. Identification of active sites

As mentioned in Section 3.2, the cobalt content (at%) presented strong positive relevance with k_{app} for Co@BC, Co@BC-N, and Co@BC-S (R^2 = 0.981, Fig. 5b), however, a moderate positive correlation was observed for Co@BC, Co@BC-N, Co@BC-S, and Co@BC-N,S (R^2 = 0.628, Fig. 5c). It revealed that the significantly heightened catalytic performance of Co@BC-N,S could be explained by the synergistic action of the doped cobalt and the modified carbon matrix by cobalt and heteroatoms. To better unravel the active sites of Co@BC-N,S and illustrate the catalytic mechanism, firstly, the changes of the chemical structure of Co@BC-N,S before and after PMS activation were investigated.

As given in Table S3, the relative amounts of O, N, S, and Co in the fresh and used Co@BC-N,S were investigated. The results indicated that each of contents of N, S, and Co decreased in varying degrees, indicating the involvement of corresponding deconvoluted structures in the catalytic process. In contrast, the content of O displayed an increase, which might be ascribed to the unavoidable oxidation of carbon matrix during the catalytic process. Although the content of O showed an increase, that of deconvoluted structures of C═O and O–C═O showed a decrease (O 1 s, Fig. 8), suggesting that groups might be the potential sites for PMS activation. It was proposed that O–C═O and C═O groups could induce the activation of PMS to produce non-radical species of $^1O_2$ (Li et al., 2021; Song et al., 2023), which was matched with the results of quenching and EPR. Moreover, the C–OH ratio increased from 44.78 % to 58.80 %, which could be explained by the hydroxyl ions or H_2O adsorbing onto catalyst (Wang et al., 2020). For the doped N, the ratio of pyridinic N (44.4 %) and graphitic N (28.3 %) dropped down to 40.55 % and 26.23 % (N 1 s, Fig. 8), respectively, while that of pyrrolic N increased from 19.67 % to 27.96 %. And the increasing content of

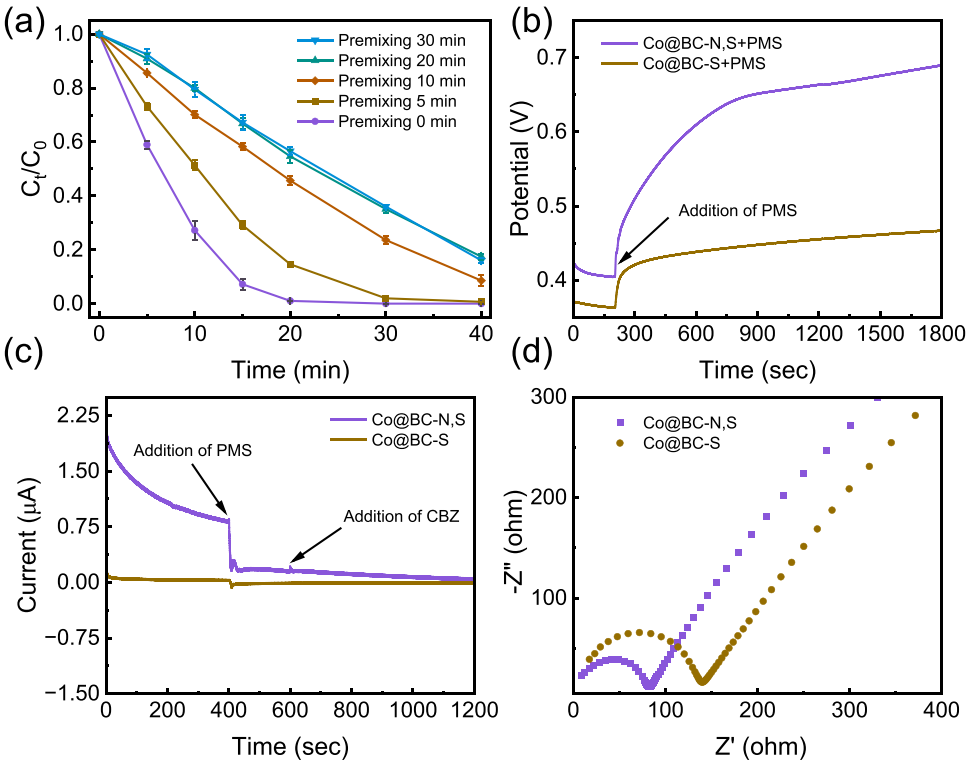

Fig. 7. (a) Effects of different premixing times on CBZ removal and (b) the OCP versus time curves, (c) i-t curves and (d) EIS Nyquist plots measured under the specified conditions with Co@BC-N,S and Co@BC-S modified electrodes as the working electrodes. Experiment conditions: [CBZ] = 2.5 mg/L, [Catalyst] = 0.1 g/L, [PMS] = 0.3 mM, and initial pH = 6.8.

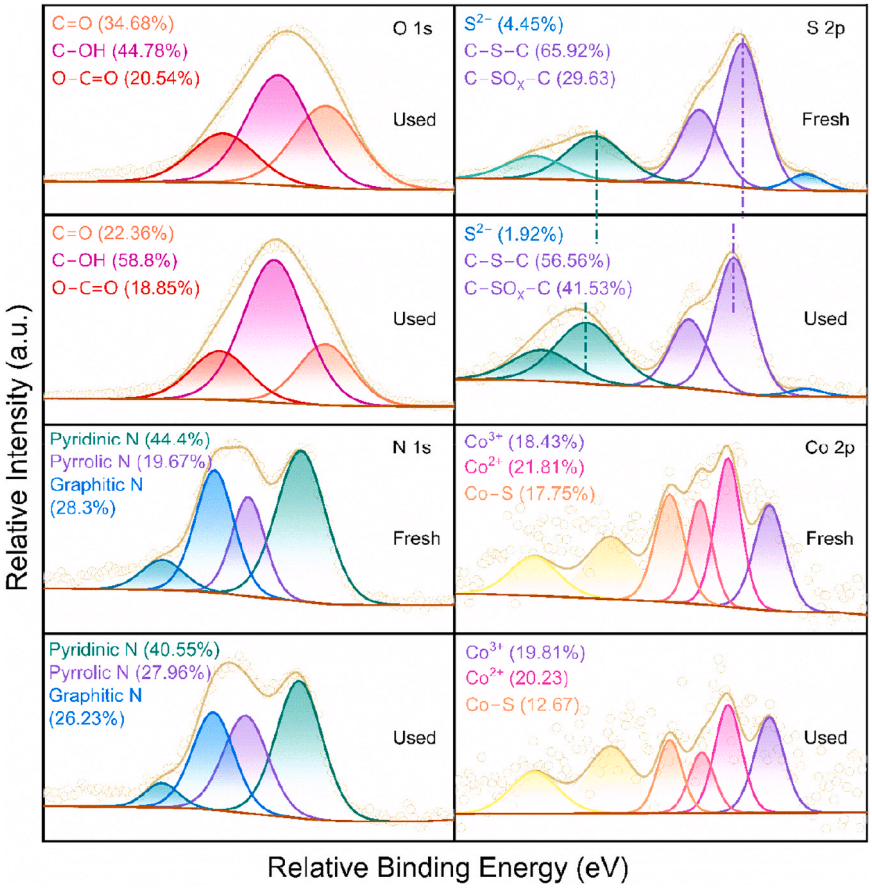

Fig. 8. The XPS spectra of O 1 s, N 1 s, S 2p, and Co 2p of Co@BC-N,S before and after reaction.

pyrrolic N could be explained by the conversion of pyridinic N to pyrrolic N (Chen et al., 2023). Prior studies revealed that doping N into carbon matrix not only could strengthen the adsorption of PMS, but also facilitate electron transfer (Wang et al., 2019; Wu et al., 2020; Li et al., 2021), which were in agreement with the great electrochemical properties of Co@BC-N,S discussed in the Section 3.3.1. For the S 2p spectra (Fig. 8), the binding energy of C–S–C and C–SO_X–C was elevated after reaction, indicating that sulfur could provide electrons during catalytic process (Wang and Wang, 2022). As previously described, moreover, the reaction between electron-rich units (C–S–C) and electrophilic O atoms of the PMS could produce •OH and $SO_4^{\bullet-}$ (Huang et al., 2021).

For the cobalt sites, Table S3 showed that the content of cobalt decreased by 13.64 %. More specifically, the peak area belonging to Co^{3+} increased from 18.43 % to 19.81 %, while those corresponding to Co^{2+} decreased from 21.81 % to 20.43 % (Co 2p, Fig. 8), indicating that the redox conversion between Co^{2+} and Co^{3+} was involved in the catalytic process. It was reported that the formation of $CoOH^+$ was the key step for Co (II)-mediated PMS activation (Eq. (1)), and the significantly heightened radio of hydroxyl ions (O 1 s, Fig. 8) might present the participation of $CoOH^+$ in PMS activation for $SO_4^{\bullet-}$ generation (Wang et al., 2020). Generally, the circulation between Co^{2+} and Co^{3+} is crucial to activate PMS for the reproduction of ROS. Hence, the efficient regeneration of Co^{2+} is also critical. In comparison with the standard reduction potential of Co^{3+}/Co^{2+} (1.81 V), whereas the standard reduction potential of S^0/S^{2-} (0.508 V) is significantly lower than that of $SO_5^{\bullet-}/HSO_5^-$ (0.81 V), hence, the conversion of Co^{3+} to Co^{2+} induced by S species is more thermodynamically favorable (Zhou et al., 2021). As shown in the fresh and used S 2p spectra (Fig. 8), the peak area of S^{2-} showed an obvious reduction after reaction, indicating that S^{2-} might participate in the reduction reaction. Therefore, the reduction of Co^{3+} to Co^{2+} in the Co@BC-N,S/PMS system might be induced by PMS as well as S^{2-} (Ding et al., 2020; Zhou et al., 2021).

3.3.3. DFT calculations

To figure out how heteroatom doping affects the structural properties and further influences PMS activation, the structures in different adsorption configurations were illustrated by density functional theory (DFT) calculations. Both experimental and characterization results confirmed the importantly catalytic role of cobalt sites. Based on the XRD and TEM analyses, the exposed facets of Co@BC-S (Co_9S_8, displayed in Fig. S12) and Co@BC-N,S (Co_4S_3, shown in Fig. 3) were constructed for calculation. The structure models of the exposed facets, adsorption structures of PMS on the corresponding facets, and the adsorption energy (E_{ads}) of PMS on the corresponding facets of Co_9S_8 and Co_4S_3 were displayed in Fig. S13 and Fig. S14, respectively. For the E_{ads}, generally, a more negative E_{ads} value means a stronger adsorption between PMS and catalyst (Zhang et al., 2021). Although Co@BC-N,S showed higher catalytic activity than Co@BC-S, the exposed facets in Co@BC-N,S (Co_4S_3) exhibited weaker adsorption compared with Co@BC-S (Co_9S_8). This result was in agreement with the results of the linear regression for cobalt contents (at%) and k_{app} of N and/or S doped Co@BC samples, further indicating that cobalt sites were more than the only origin of the excellent catalytic performance of Co@BC-N,S.

In addition to cobalt sites, the enhanced catalytic performance of Co@BC-N,S might be ascribed to the synergistic roles between Co_4S_3 and the N and S doped biochar. To make this point, we further constructed the metal@graphene hybrid models for Co@BC-S (Co_9S_8@SG) and Co@BC-N,S (Co_4S_3@NSG) as well as the corresponding PMS adsorption configurations (Fig. 9). It was found that Co_4S_3@NSG significantly raise the PMS adsorption ($E_{ads} = -3.64$ eV) in comparison with Co_9S_8@SG ($E_{ads} = -1.07$ eV), indicating that the synergistic effect between Co_4S_3 and the N-S modified carbon could enhance the

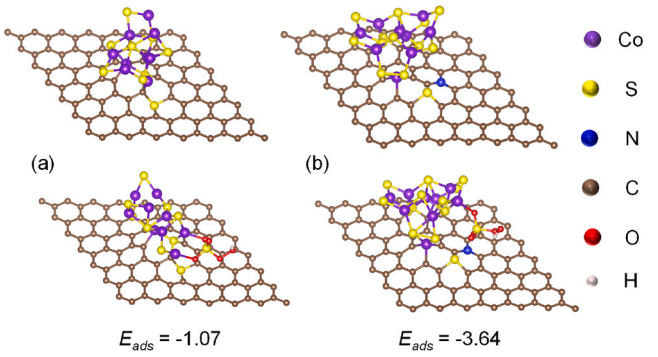

Fig. 9. DFT configurations of PMS adsorption onto (a) Co_9S_8@SG and (b) Co_4S_3@NSG.

interactions between Co@BC-N,S and PMS, which was in line with the above experimental results. Overall, both the results of experiment and DFT calculation disclosed that the excellent catalytic performance of Co@BC-N,S was ascribed not only to cobalt sites but also the synergistic effect between Co_4S_3 and the N-S modified carbon matrix, which induced Co@BC-N,S to activate PMS into radical and non-radical pathways.

3.3.4. Proposed activation mechanism

Upon the aforementioned analysis, the possible CBZ degradation mechanism in Co@BC-N,S/PMS system was described in Fig. 10. Both radical and non-radical oxidation pathways were responsible for catalytic degradation of CBZ. In the radical pathway, Co^{2+} in catalysts firstly combined with H_2O to generate $CoOH^+$ (Eq. (1)), which was the crucial step in PMS activation. Then, PMS could be activated to produce $SO_4^{\bullet-}$ via an electron transfer from $CoOH^+$ to PMS (Eq. (2)), and Co^{2+} was oxidized to Co^{3+} in the meantime. Here, the conversion of Co^{3+} to Co^{2+} could be induced by HSO_5^- (Eq. (4)) and S^{2-} (Eq. (5)). The generation processes of •OH and $O_2^{\bullet-}$ could be described by the Eqs. (6–9), and Eq. (10) might be another pathway for the formation of $SO_4^{\bullet-}$. Furthermore, the reaction between the C–S–C groups and the electrophilic O in PMS could promote the generation of $SO_4^{\bullet-}$ and •OH.

$$Co^{2+} + H_2O \leftrightarrow CoOH^+ + H^+ \quad (1)$$

$$CoOH^+ + HSO_5^- \rightarrow CoO^+ + SO_4^{\bullet-} + H_2O \quad (2)$$

$$CoO^+ + 2H^+ \leftrightarrow Co^{3+} + H_2O \quad (3)$$

$$Co^{3+} + HSO_5^- \rightarrow Co^{2+} + SO_5^{\bullet-} + H^+ \quad (4)$$

$$2Co^{3+} + 2S^{2-} \rightarrow 2Co^{2+} + S_2^{2-} \quad (5)$$

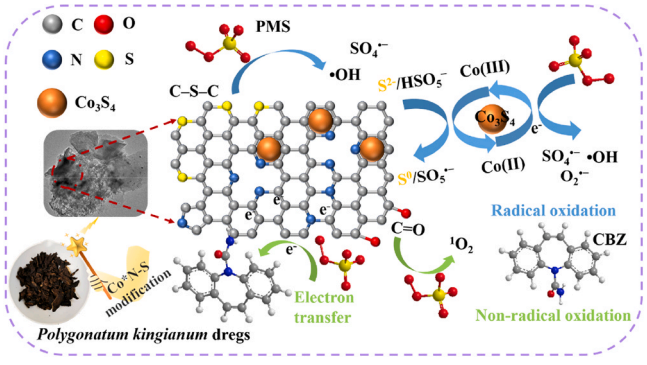

Fig. 10. Proposed mechanism of the Co@BC-N,S/PMS system for CBZ degradation.

$$SO_4^{\bullet-} + H_2O \rightarrow SO_4^{2-} + H^+ + {}^{\bullet}OH \quad (6)$$

$$SO_4^{\bullet-} + OH^- \rightarrow SO_4^{2-} + {}^{\bullet}OH \quad (7)$$

$$HSO_5^- \rightarrow SO_5^{2-} + H^+ \quad (8)$$

$$SO_5^{2-} + H_2O \rightarrow SO_4^{2-} + O_2^{\bullet-} + 2H^+ \quad (9)$$

$$HSO_5^- + O_2^{\bullet-} \rightarrow SO_4^{\bullet-} + O_2 + OH^- \quad (10)$$

$$HSO_5^- \rightarrow SO_5^{\bullet-} + H^+ + e^- \quad (11)$$

$$4SO_5^{\bullet-} + 2H_2O \rightarrow 4HSO_4^- + 3O_2^1 \quad (12)$$

$$2O_2^{\bullet-} + 2H_2O \rightarrow O_2^1 + H_2O_2 + 2OH^- \quad (13)$$

On the other hand, Co@BC-N,S presented a better affinity for PMS and the higher electron transfer ability, thus inducing the degradation of CBZ via ETP. During the process, PMS was firstly bounded onto Co@BC-N,S and activated to form PMS/Co@BC-N,S complex, possessing a higher redox potential. Then, the adsorbed CBZ could be oxidized by donating electrons via carbon matrix to the complex. In addition, the production of $^1O_2$ was derived from $SO_5^{\bullet-}$ and $O_2^{\bullet-}$ (Eqs. (11)–(13)) as well as the reaction between C═O groups and PMS (Eqs. (14–17)).

3.4. Adaptability and reusability

The effects of initial pH and coexisted substrates on the catalytic performance of the Co@BC-N,S/PMS system were investigated to evaluate its potential applications. As for the pH, Fig. 11a showed that Co@BC-N,S/PMS system possessed good removal rate in the initial pH from 5 to 9. However, the CBZ removal was significantly impeded at pH of 3 and 11. At the condition of strong acid, excessive H^+ might consume radicals. Furthermore, the interaction between H^+ and PMS might induce the formation of hydrogen bond, leading it difficult to break O–O–O in PMS. Which could hamper the production of ROS and lead to poor CBZ removal (Song et al., 2023; Zhou et al., 2023). As for pH of 11, $SO_4^{\bullet-}$ and •OH might be quenched by excessive OH^-, thus resulting poor CBZ degradation (Zhou et al., 2023).

The influences of coexisted substrates were displayed in Fig. S15. The concentration of NO_3^- and SO_4^{2-}, ranging from 2 to 5 mM, showed a negligible impeding effect (Fig. S15a and b). Surprisingly, the HPO_4^{2-} markedly promoted the catalytic efficiency (Fig. S15c), which might be ascribed to the fact that phosphate could activate PMS to generate more free radicals (Wen et al., 2022). Fig. S15d showed that the removal of CBZ was hindered by Cl^- opposite to concentration. Specifically, low concentration was more inhibitory than the high. The CBZ removal efficiency was increased gradually from 76.6 % to 98.3 % with raising the concentration of Cl^- from 2 to 15 mM. The slight impeding effect might be explained by the quenching reaction between Cl^- and $SO_4^{\bullet-}$/•OH, generating $Cl^{\bullet}$ and $Cl_2^{\bullet-}$ with lower redox potentials. While the clearly boosted catalytic process might be ascribed to the direct reaction between PMS and Cl^-, producing a large amount of non-radical species (HOCl) (Peng et al., 2021).

The removal efficiency of CBZ dropped down to 94.3 % and 49.7 %, within 40 min, respectively for the addition of 2 and 5 mM HCO_3^- (Fig. S15e). The reduction of the removal efficiency might be explained by the fact that high level of HCO_3^- (> 4 mM) could observably quench •OH and $SO_4^{\bullet-}$ (Qin et al., 2022). As for humic acid (HA), Fig. S15f displayed that the CBZ removal property was little changed in the presence of 1 mg/L HA. While it decreased gradually with the HA concentration increasing from 1 to 10 mg/L. Therefore, Co@BC-N,S/PMS system had good tolerance to common anions and HA upon the concertation of environmental matrix.

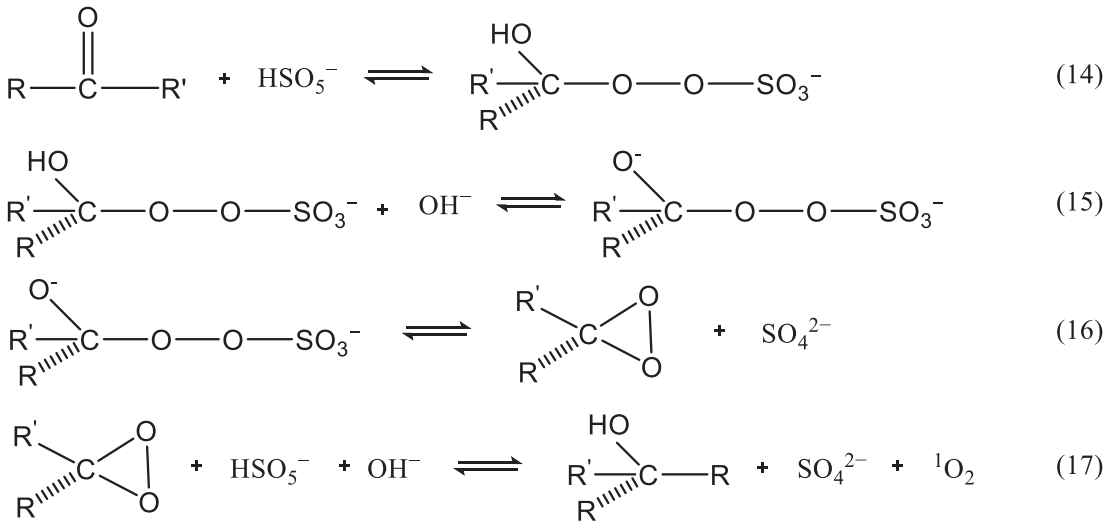

(14)

(15)

(16)

(17)

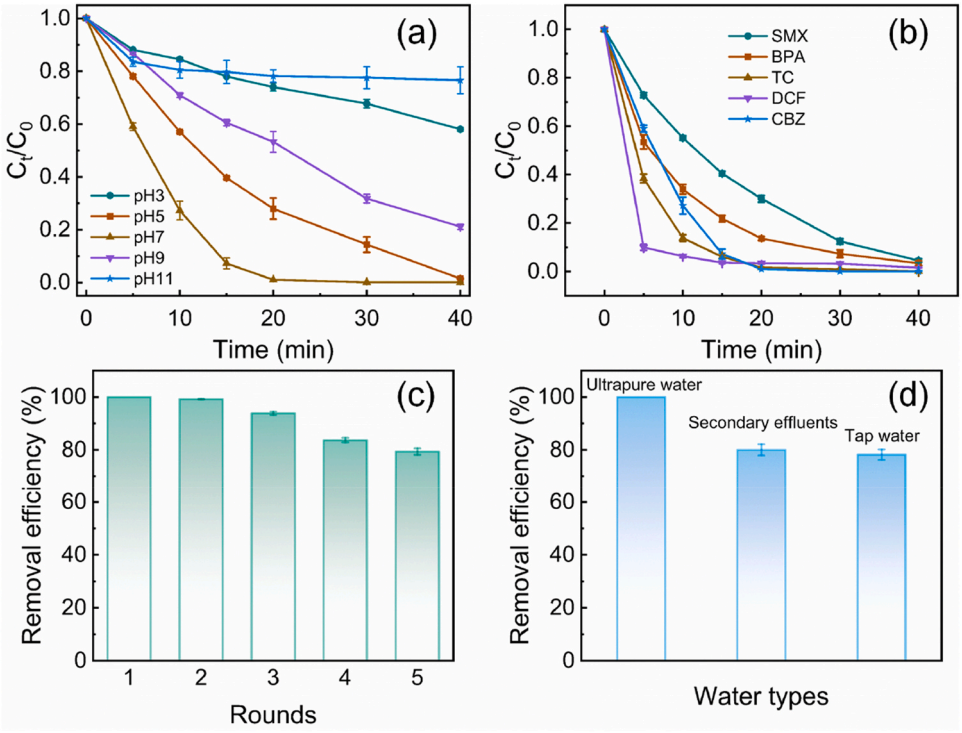

Fig. 11. (a) Effects of different pH on CBZ degradation, (b) degradation of various pollutants in the Co@BC-N,S/PMS system, (c) recyclability of Co@BC-N,S for CBZ removal, and (d) water types on CBZ removal efficiency. Experiment conditions: [CBZ] = 2.5 mg/L, [Catalyst] = 0.1 g/L, [PMS] = 0.3 mM, and initial pH = 6.8.

To further investigate the adaptability of the Co@BC-N,S/PMS system in environmental waters, it was applied in tap water and secondary effluent for CBZ removal (Fig. 11d). The details of secondary effluent were listed in Table S4. It displayed that the system could achieve good degradation performances (80 %) in both tap water and secondary effluent, implying the great effectiveness of the system in actual water body. Moreover, the catalytic performances of this system to other emerging compounds were also examined, including sulfamethoxazole (SMX), bisphenol A (BPA), tetracycline (TC), and diclofenac (DCF). Fig. 11b and S16 demonstrated that the Co@BC-N,S/PMS system could also achieve great removal performance to other emerging pollutants by catalytic degradation. Furthermore, the reusability of Co@BC-N,S was studied. As displayed in Fig. 11c, the Co@BC-N,S possessed good degradation efficiencies in five cycles, suggesting the good reusability of it. Upon the analyzed results, the Co@BC-N,S prepared in this work with multiple catalytic oxidation pathways, outstanding adaptability, and excellent reusability is a promising catalyst for catalytic decontamination. Moreover, the raw materials for preparing Co@BC-N,S is mainly from the biomass wastes of *Polygonatum kingianum* (PK) dregs with no cost. The main preparation cost of Co@BC-N,S is from the pyrolysis process. But it is still lower than the metal-based catalysts. Hence, the low cost and excellent performances are promise in the environmental application. However, substantially more research and long-term studies are necessary to assess the application potential and cost of large-scale biochar implementation.

4. Conclusion

A series of Co@BC hybrids were synthesized with no doping and the doping of N, S, and N-S, and employed to activate PMS for the removal of CBZ. Results indicated that N doping was negative whilst S doping was positive for the catalytic activity of Co@BC. Upon the co-doping of N-S, an outstanding synergistic effect was presented between Co_4S_3 and the N-S modified carbon matrix, which significantly raised the PMS adsorption (E_{ads} = –3.64 eV). As a result, PMS could be effectively activated by Co@BC-N,S into non-radical pathways ($^1O_2$ and ETP) and radical pathways ($SO_4^{\bullet-}$, •OH, and $O_2^{\bullet-}$) for catalytic decontamination of CBZ. Particularly, the Co@BC-N,S calcinated at 700 ℃ exhibited proper thickness of carbon layer and good catalytic stability. Under the optimal reaction conditions, 100 % degradation efficiency of CBZ was obtained in the Co@BC-N,S/PMS system, which also presented excellent catalytic activity in the range of pH= 5–9, as well as good tolerance to NO_3^-, SO_4^{2-}, HPO_4^{2-}, Cl^-, HCO_3^-, and HA based on the concertation of environmental matrix. And the effectiveness was also confirmed by the high removal efficiency of CBZ in the actual water body. Furthermore, Co@BC-N,S possessed great recycling effect and displayed excellent degradation performance on other types of emerging pollutants. Consequently, this research provides the new insights into the roles of N or/and S doping in modifying the structural properties of Co@BC hybrid for PMS activation as well as the utilization of *Polygonatum kingianum* dregs in catalytic decontamination.

CRediT authorship contribution statement

xiaoya Gao: Writing – review & editing, Supervision, Funding acquisition. **Min Li:** Resources, Investigation. **Wei Li:** Resources, Methodology. **Xingxin Yang:** Writing – review & editing, Resources, Investigation. **Weimei Yu:** Resources, Investigation. **Jinli Zhai:** Supervision, Methodology. **Fali Hou:** Writing – original draft, Visualization, Software, Formal analysis, Data curation, Conceptualization. **Kaiying Yang:** Resources, Methodology. **Jiali Yan:** Supervision, Methodology.

Declaration of Competing Interest

The authors declare that they have no known competing financial interests or personal relationships that could have appeared to influence the work reported in this paper.

Acknowledgements

This work was supported by the National Natural Science Foundation of China (42367060, 42067057), the Basis Research Project of Yunnan China (Grants 202101AT070087), and the High-level Scientific Research Foundation for Talent Introduction of Kunming University of Science and Technology (10978172).

Appendix A. Supporting information

Supplementary data associated with this article can be found in the online version at doi:10.1016/j.indcrop.2024.120317.

Data Availability

Data will be made available on request.

References

Chen, X., Guo, Z., Liu, J., Wu, F., Cheng, C., Lin, H., Ren, W., Zhang, H., 2023. Electron transfer-based peroxydisulfate activation by waste herb residue biochar: adsorption versus surface oxidation. Chem. Eng. J. 451, 138560.
Chen, W., Lei, L., Zhu, K., He, D., He, H., Li, X., Wang, Y., Huang, J., Ai, Y., 2023. Peroxymonosulfate activation by Fe-N-S co-doped tremella-like carbocatalyst for degradation of bisphenol a: Synergistic effect of pyridine N, Fe-N, thiophene S. J. Environ. Sci. 129, 213–228.
Clara, M., Strenn, B., Kreuzinger, N., 2004. Carbamazepine as a possible anthropogenic marker in the aquatic environment: investigations on the behaviour of Carbamazepine in wastewater treatment and during groundwater infiltration. Water Res 38 (4), 947–954.
Dai, X., Li, Z., Ma, Y., Liu, M., Du, K., Su, H., Zhuo, H., Yu, L., Sun, H., Zhang, X., 2016. Metallic cobalt encapsulated in bamboo-like and nitrogen-rich carbonitride nanotubes for hydrogen evolution reaction. ACS Appl. Mater. Interfaces 8 (10), 6439–6448.
Ding, Y., Hu, Y., Peng, X., Xiao, Y., Huang, J., 2020. Micro-nano structured CoS: an efficient catalyst for peroxymonosulfate activation for removal of bisphenol a. Sep. Purif. Technol. 233, 116022.
Dou, J., Cheng, J., Lu, Z., Tian, Z., Xu, J., He, Y., 2022. Biochar co-doped with nitrogen and boron switching the free radical based peroxydisulfate activation into the electron-transfer dominated nonradical process. Appl. Catal. B Environ. 301, 120832.
Du, W., Zhang, Q., Shang, Y., Wang, W., Li, Q., Yue, Q., Gao, B., Xu, X., 2020. Sulfate saturated biosorbent-derived Co-S@NC nanoarchitecture as an efficient catalyst for peroxymonosulfate activation. Appl. Catal. B Environ. 262, 118302.
Duan, X., O'Donnell, K., Sun, H., Wang, Y., Wang, S., 2015. Sulfur and nitrogen co-doped graphene for metal-free catalytic oxidation reactions. Small 11 (25), 3036–3044.
Dung, N.T., Thao, V.D., Thao, N.P., Thuy, C.T.M., Nam, N.H., Ngan, L.V., Lin, K.A., Khiem, T.C., Huy, N.N., 2024. Turning peroxymonosulfate activation into singlet oxygen-dominated pathway for ofloxacin degradation by co-doping N and S into durian peel-derived biochar. Chem. Eng. J. 483, 149099.
Feng, X., Xiao, Z., Shi, H., Zhou, B., Wang, Y., Chi, H., Kou, X., Ren, N., 2022. How nitrogen and sulfur doping modified material structure, transformed oxidation pathways, and improved degradation performance in peroxymonosulfate activation. Environ. Sci. Technol. 56 (19), 14048–14058.
He, S., Wang, X., Chen, J., Li, X., Gu, W., Zhang, F., Cao, G., Yu, J., 2022. Optimization of the ultrasonic-assisted extraction technology of steroidal saponins from Polygonatum kingianum collett & hemsl and evaluating its quality planted in different areas. Molecules 27 (5), 1463.
Hodges, B.C., Cates, E.L., Kim, J., 2018. Challenges and prospects of advanced oxidation water treatment processes using catalytic nanomaterials. Nat. Nanotechnol. 13 (8), 642–650.
Hristea, G., Iordoc, M., Lungulescu, E., Bejenari, I., Volf, I., 2024. A sustainable bio-based char as emerging electrode material for energy storage applications. Sci. Rep. 14 (1).
Huang, M., Wang, X., Liu, C., Fang, G., Gao, J., Wang, Y., Zhou, D., 2021. Facile ball milling preparation of sulfur-doped carbon as peroxymonosulfate activator for efficient removal of organic pollutants. J. Environ. Chem. Eng. 9 (6), 106536.
Huang, X., Yu, Z., Shi, Y., Liu, Q., Fang, S., 2022. Highly efficient activation of peroxymonosulfate by Co, S co-doped bamboo biochar for sulfamethoxazole degradation: insights into the role of S. J. Environ. Chem. Eng. 10 (5), 108380.
Li, N., Li, R., Duan, X., Yan, B., Liu, W., Cheng, Z., Chen, G., Hou, L.A., Wang, S., 2021. Correlation of active sites to generated reactive species and degradation routes of organics in peroxymonosulfate activation by co-loaded carbon. Environ. Sci. Technol. 55 (23), 16163–16174.
Li, W., Li, S., Tang, Y., Yang, X., Zhang, W., Zhang, X., Chai, H., Huang, Y., 2020. Highly efficient activation of peroxymonosulfate by cobalt sulfide hollow nanospheres for fast ciprofloxacin degradation. J. Hazard. Mater. 389, 121856.
Li, N., Ye, J., Dai, H., Shao, P., Liang, L., Kong, L., Yan, B., Chen, G., Duan, X., 2023. A critical review on correlating active sites, oxidative species and degradation routes with persulfate-based antibiotics oxidation. Water Res. 235, 119926.
Liu, J., Jiang, J., Wang, M., Kang, J., Zhang, J., Liu, S., Tang, Y., Li, S., 2022. Peroxymonosulfate activation by cobalt particles embedded into biochar for levofloxacin degradation: efficiency, stability, and mechanism. Sep. Purif. Technol. 294, 121082.
Ma, B., Li, B., Li, Y., Fan, X., Zhang, F., Zhang, G., Zhu, Y., Peng, W., 2021. Synthesis of nitrogen and sulfur co-doped carbon with special hollow sphere structure for enhanced catalytic oxidation. Sep. Purif. Technol. 278, 119522.
Miao, J., Geng, W., Alvarez, P.J.J., Long, M., 2020. 2D N-doped porous carbon derived from polydopamine-coated graphitic carbon nitride for efficient nonradical activation of peroxymonosulfate. Environ. Sci. Technol. 54 (13), 8473–8481.
Mu, J., Zi, L., Li, Y., Yu, L., Cui, Z., Shi, T., Zhang, F., Gu, W., Hao, J., Yu, J., Yang, X., 2021. Jiuzhuan Huangjing Pills relieve mitochondrial dysfunction and attenuate high-fat diet-induced metabolic dysfunction-associated fatty liver disease. Biomed. Pharmacother. 142, 112092.
Navarro Pardo, F., Liu, J., Abdelkarim, O., Selopal, G.S., Yurtsever, A., Tavares, A.C., Zhao, H., Wang, Z.M., Rosei, F., 2020. 1D/2D cobalt-based nanohybrids as electrocatalysts for hydrogen generation. Adv. Funct. Mater. 30 (14).
Otor, H.O., Steiner, J.B., García-Sancho, C., Alba-Rubio, A.C., 2020. Encapsulation methods for control of catalyst deactivation: a review. ACS Catal. 10 (14), 7630–7656.
Peng, L., Shang, Y., Gao, B., Xu, X., 2021. Co_3O_4 anchored in N, S heteroatom co-doped porous carbons for degradation of organic contaminant: role of pyridinic N-Co binding and high tolerance of chloride. Appl. Catal. B: Environ. 282, 119484.
Qin, Y., Li, X., Wang, L., Luo, J., Li, Y., Yao, C., Xiao, Z., Zhai, S., An, Q., 2022. Valuable cobalt/biochar with enriched surface oxygen-containing groups prepared from bio-waste shrimp shell for efficient peroxymonosulfate activation. Sep. Purif. Technol. 281, 119901.
Qu, J., Xu, Y., Zhang, X., Sun, M., Tao, Y., Zhang, X., Zhang, G., Ge, C., Zhang, Y., 2022. Ball milling-assisted preparation of N-doped biochar loaded with ferrous sulfide as persulfate activator for phenol degradation: multiple active sites-triggered radical/non-radical mechanism. Appl. Catal. B Environ. 316, 121639.

Ren, W., Cheng, C., Shao, P., Luo, X., Zhang, H., Wang, S., Duan, X., 2022. Origins of electron-transfer regime in persulfate-based nonradical oxidation processes. Environ. Sci. Technol. 56 (1), 78–97.
Sajjadi, B., Shrestha, R.M., Chen, W., Mattern, D.L., Hammer, N., Raman, V., Dorris, A., 2021. Double-layer magnetized/functionalized biochar composite: role of microporous structure for heavy metal removals. J. Water Process. Eng. 39, 101677.
Shi, Q., Deng, S., Zheng, Y., Du, Y., Li, L., Yang, S., Zhang, G., Du, L., Wang, G., Cheng, M., Liu, Y., 2022. The application of transition metal-modified biochar in sulfate radical based advanced oxidation processes. Environ. Res. 212, 113340.
Song, J., Zhao, C., Cao, X., Cheng, W., 2023. Enhanced catalytic degradation of antibiotics by peanut shell-derived biochar-Co_3O_4 activated peroxymonosulfate: an experimental and mechanistic study. Process Saf. Environ. Prot. 171, 423–436.
Tam, N.T.M., Liu, Y., Bashir, H., Zhang, P., Liu, S., Tan, X., Dai, M., Li, M., 2020. Synthesis of porous biochar containing graphitic carbon derived from lignin content of forestry biomass and its application for the removal of diclofenac sodium from aqueous solution. Front. Chem. 8.
Tang, L., Meng, X., Deng, D., Bao, X., 2019. Confinement catalysis with 2D materials for energy conversion. Adv. Mater. 31 (50).
Wacławek, S., Lutze, H.V., Grübel, K., Padil, V.V.T., erník, M., Dionysiou, D.D., 2017. Chemistry of persulfates in water and wastewater treatment: a review. Chem. Eng. J. 330, 44–62.
Wang, S., Liu, H., Wang, J., 2020. Nitrogen, sulfur and oxygen co-doped carbon-armored Co/Co_9S_8 rods (Co/Co_9S_8@N-S-O-C) as efficient activator of peroxymonosulfate for sulfamethoxazole degradation. J. Hazard. Mater. 387, 121669.
Wang, G., Nie, X., Ji, X., Quan, X., Chen, S., Wang, H., Yu, H., Guo, X., 2019. Enhanced heterogeneous activation of peroxymonosulfate by Co and N codoped porous carbon for degradation of organic pollutants: the synergism between Co and N. Environ. Sci. Nano 6 (2), 399–410.
Wang, S., Wang, J., 2020. Peroxymonosulfate activation by Co_9S_8@ S and N co-doped biochar for sulfamethoxazole degradation. Chem. Eng. J. 385, 123933.
Wang, S., Wang, J., 2022. High efficient activation of peroxymonosulfate by Co_9S_8 anchored in N, S, O co-doped carbon composite for degradation of sulfamethoxazole: effect of sulfur precursor and sulfur doping content. Chem. Eng. J. 434, 134824.
Wen, Y., Sharma, V.K., Ma, X., 2022. Activation of peroxymonosulfate by phosphate and carbonate for the abatement of Atrazine: roles of radical and nonradical species. ACS EST Water 2 (4), 635–643.
Wu, S., Liu, H., Yang, C., Li, X., Lin, Y., Yin, K., Sun, J., Teng, Q., Du, C., Zhong, Y., 2020. High-performance porous carbon catalysts doped by iron and nitrogen for degradation of bisphenol F via peroxymonosulfate activation. Chem. Eng. J. 392, 123683.
Wu, W., Wang, R., Chang, H., Zhong, N., Zhang, T., Wang, K., Ren, N., Ho, S., 2023. Rational electron tunning of magnetic biochar via N, S co-doping for intense tetracycline degradation: efficiency improvement and toxicity alleviation. Chem. Eng. J. 458, 141470.
Wu, Z., Xiong, Z., Liu, R., He, C., Liu, Y., Pan, Z., Yao, G., Lai, B., 2022. Pivotal roles of N-doped carbon shell and hollow structure in nanoreactor with spatial confined Co species in peroxymonosulfate activation: obstructing metal leaching and enhancing catalytic stability. J. Hazard. Mater. 427, 128204.
Xiao, Z., Feng, X., Shi, H., Zhou, B., Wang, W., Ren, N., 2022. Why the cooperation of radical and non-radical pathways in PMS system leads to a higher efficiency than a single pathway in tetracycline degradation. J. Hazard. Mater. 424, 127247.
Xie, J., Zhang, L., Luo, X., Huang, L., Gong, X., Tian, J., 2023. Sulfur anchored on N-doped porous carbon as metal-free peroxymonosulfate activator for tetracycline hydrochloride degradation: nonradical pathway mechanism, performance and biotoxicity. Chem. Eng. J. 457, 141149.
Xu, R., Wei, J., Cheng, D., Wang, W., Hong, L., Chen, Y., Guo, Y., 2024. Abundant porous biochar derived from luffa vine for removal of methylene blue: selective adsorption and mechanistic studies. Ind. Crop. Prod. 219, 119114.
Yan, Y., Wei, Z., Duan, X., Long, M., Spinney, R., Dionysiou, D.D., Xiao, R., Alvarez, P.J. J., 2023. Merits and limitations of radical vs. nonradical pathways in persulfate-based advanced oxidation processes. Environ. Sci. Technol. 57 (33), 12153–12179.
Yang, Q., Chen, Y., Duan, X., Zhou, S., Niu, Y., Sun, H., Zhi, L., Wang, S., 2020. Unzipping carbon nanotubes to nanoribbons for revealing the mechanism of nonradical oxidation by carbocatalysis. Appl. Catal. B Environ. 276, 119146.
Yang, X., Wang, X., Shi, T., Dong, J., Li, F., Zeng, L., Yang, M., Gu, W., Li, J., Yu, J., 2019. Mitochondrial dysfunction in high-fat diet-induced nonalcoholic fatty liver disease: the alleviating effect and its mechanism of Polygonatum kingianum. Biomed. Pharmacother. 117, 109083.
Yu, L., Deng, D., Bao, X., 2020. Chain mail for catalysts. Angew. Chem. Int. Ed. 59 (36), 15294–15297.
Yu, J., Tang, L., Pang, Y., Zeng, G., Feng, H., Zou, J., Wang, J., Feng, C., Zhu, X., Ouyang, X., Tan, J., 2020. Hierarchical porous biochar from shrimp shell for persulfate activation: a two-electron transfer path and key impact factors. Appl. Catal. B Environ. 260, 118160.
Zhang, X., Yan, X., Hu, X., Feng, R., Zhou, M., Wang, L., 2022. Efficient removal of organic pollutants by a Co/N/S-doped yolk-shell carbon catalyst via peroxymonosulfate activation. J. Hazard. Mater. 421, 126726.
Zhang, P., Yang, Y., Duan, X., Liu, Y., Wang, S., 2021. Density functional theory calculations for insight into the heterocatalyst reactivity and mechanism in persulfate-based advanced oxidation reactions. ACS Catal. 11 (17), 11129–11159.
Zhang, P., Zhang, H., Wu, M., Li, Y., Xia, W., Zhu, X., Zhang, W., 2024. Physicochemical properties, antioxidant and cardioprotective activities of polysaccharides from fermented Polygonatum kingianum with Lactobacillus species. Ind. Crop. Prod. 216, 118699.
Zhao, H., Liu, X., Liu, Y., Wu, D., Hu, W., Shang, X., Lv, M., 2023. Directionally inducing non-radical pathways for peroxymonosulfate activation by regulating the exposed crystal plane of MnO_2. Process Saf. Environ. Prot. 177, 947–958.
Zhou, X., Luo, M., Xie, C., Wang, H., Wang, J., Chen, Z., Xiao, J., Chen, Z., 2021. Tunable S doping from Co_3O_4 to Co_9S_8 for peroxymonosulfate activation: distinguished Radical/Nonradical species and generation pathways. Appl. Catal. B Environ. 282, 119605.
Zhou, J., Yang, X., Wei, Q., Lan, Y., Guo, J., 2023. Co_3O_4 anchored on biochar derived from chitosan (Co_3O_4@BCC) as a catalyst to efficiently activate peroxymonosulfate (PMS) for degradation of phenacetin. J. Environ. Manag. 327, 116895.
Zhu, J., Yan, L., Li, X., Song, W., Yan, T., Li, Y., 2023. Ball-milled MoS2/biochar as peroxymonosulfate activator efficiently removes tetracycline: multiple active sites-triggered radical/non-radical pathways. Ind. Crop. Prod. 205, 117450.